

# Modeling Fast Electron Dynamics with Real-Time Time-Dependent Density Functional Theory: Application to Small Molecules and Chromophores

Kenneth Lopata\* and Niranjana Govind\*

William R. Wiley Environmental Molecular Sciences Laboratory, Pacific Northwest National Laboratory

**ABSTRACT:** The response of matter to external fields forms the basis for a vast wealth of fundamental physical processes ranging from light harvesting to nanoscale electron transport. Accurately modeling ultrafast electron dynamics in excited systems thus offers unparalleled insight but requires an inherently nonlinear time-resolved approach. To this end, an efficient and massively parallel real-time real-space time-dependent density functional theory (RT-TDDFT) implementation in NWChem is presented. The implementation is first validated against linear-response TDDFT and experimental results for a series of molecules subjected to small electric field perturbations. Second, nonlinear excitation of green fluorescent protein is studied, which shows a blue-shift in the spectrum with increasing perturbation, as well as a saturation in absorption. Next, the charge dynamics of optically excited zinc porphyrin is presented in real time and real space, with relevance to charge injection in photovoltaic devices. Finally, intermolecular excitation in an adenine-thymine base pair is studied using the BNL range separated functional [Baer, R.; Neuhauser, D. *Phys. Rev. Lett.* **2005**, *94*, No. 043002], demonstrating the utility of a real-time approach in capturing charge transfer processes.

## 1. INTRODUCTION

The time-dependent response of molecules under external fields forms the basis of a host of fundamental physical processes including light harvesting, photodissociation, electron transport, and higher harmonic emission. Broadly, radiation–molecule interactions can be classified as either weak or strong. When the interaction with the field is much smaller than the intramolecular interactions, the excitation is weak and the field induces only a small perturbation from the ground state. Perturbation theories such as linear-response time-dependent density functional theory (LR-TDDFT)<sup>1–3</sup> are excellent at modeling weak excitations and can accurately predict properties such as the absorption spectra of molecules and materials.<sup>4</sup> In the general case, however, matter–radiation interactions require going beyond linear response.

A fundamental understanding of nonlinear excited state dynamics at the femto- and subfemtosecond time regimes offers unparalleled insight into unsolved problems such as nonlinear spectra of single molecules, the nature of photoabsorption and exciton dynamics in photovoltaic devices, transport through molecules, and many others. Modeling nonlinear dynamics at molecular length scales, however, is a challenge requiring a combination of careful theoretical formulation and considerable computational effort. Unlike the weak excitation limit, where frequency domain perturbative approaches suffice, the strong excitation regime involves a complex interplay of electronic and nuclear dynamics and is best captured with a real-time, real-space approach. Here, the electron density, and in some cases nuclear motion, is monitored in time and space, which sheds light directly on the fundamental mechanisms of the excitation. Moreover, fully nonlinear (beyond perturbation theory) spectral information is readily obtainable from a real-time simulation via Fourier transform of time-dependent expectation values, such as the dipole moment.

All this comes at a cost, and studying real-time dynamics in molecules and materials is a daunting task. In particular, evolving a system in time requires calculating these potentials at every time step, which is extremely time-consuming. Additionally, care must be taken in evolving the system in time, and propagators must strike a balance between accuracy, stability, and speed. Finally, since excited states tend to be quite delocalized, dynamics simulations typically require the use of larger basis sets compared to traditional ground state calculations.

Despite the challenges, many successful approaches have been developed to study real-time electron dynamics in realistic systems. Within the Born–Oppenheimer approximation, these include: direct integration of the Schrödinger equation for very small systems (e.g., H<sub>2</sub>);<sup>5</sup> real-time configuration interaction singles (CIS);<sup>6,7</sup> real-time orbital-free/Thomas-Fermi;<sup>8,9</sup> real-time, time-dependent density functional theory (RT-TDDFT) (discussed below); real-time Hartree–Fock (RT-TDHF);<sup>10,11</sup> and time-dependent semiempirical methods (e.g., TD-PM3).<sup>12</sup> DFT in particular offers a good trade-off between accuracy and efficiency for both ground and excited states, which has motivated extensive interest in TDDFT for real-time modeling, of which we present a representative sampling below.

Real-space (grid-based), time-dependent local density approximation RT-TDDFT, which was first developed by Theilhaber,<sup>13</sup> and pioneered by Yabana and Bertsch,<sup>14</sup> has been applied to systems ranging from aluminum dimers<sup>15</sup> to quantum dots in magnetic fields.<sup>16</sup> The Octopus<sup>17</sup> real-time TDDFT package derives from this lineage. Real-time TD-LDA using a planewave basis has similarly been applied to aluminum dimers,<sup>18</sup> modeling enhanced absorption of a nanoshell,<sup>19</sup> and conduction through a molecular junction.<sup>20</sup> RT-TDDFT has also been performed with

Received: February 23, 2011

Published: April 19, 2011

numerical orbitals using Siesta,<sup>21</sup> applied to atomic clusters<sup>22</sup> and higher harmonic generation in chromophores,<sup>23</sup> and extended to include ionic motion.<sup>24</sup> Another approach is to use a tight binding Hamiltonian for RT-TDDFT,<sup>25</sup> for which linear scaling implementations have been used to study absorption spectra.<sup>26</sup> Finally, RT-TDDFT with an atom-centered Gaussian basis has been used to study molecular conductance,<sup>27,28</sup> excited states at metal surfaces,<sup>29</sup> absorption properties of silicon clusters,<sup>30</sup> and double excitations<sup>31</sup> and singlet–triplet transitions.<sup>32</sup>

There has also been extensive work in developing schemes which go beyond the Born–Oppenheimer approximation to explicitly treat nuclear motion such as Ehrenfest dynamics,<sup>33–35</sup> Liouville–von Neumann molecular dynamics with real-time tight binding,<sup>36</sup> using surface hopping<sup>37</sup> to emulate nonadiabatic switching between adiabatic states,<sup>38–40</sup> and correlated electron–ion dynamics.<sup>41</sup>

In this paper, we present a massively parallel RT-TDDFT implementation in NWChem<sup>42</sup> geared towards simulating large systems while still maintaining generality and flexibility (e.g., various basis sets and functionals) and use it to explore the linear and nonlinear response properties of a series of molecules. The remainder of the paper takes the following form: The overall methodology is outlined in section 2.1. The structure of the time-dependent complex Fock matrix is discussed in section 2.2. The propagation scheme is detailed in section 2.3, and section 2.4 highlights some of the computation considerations. Next, the scheme is validated against LR-TDDFT for a few small molecules in section 3.1. The nonlinear absorption properties of the green fluorescent protein (GFP) are explored in section 3.2. Real-time, real-space visualization of resonant excitation in zinc porphyrin is presented in section 3.3, and finally, intramolecular charge transfer excitation in the adenine–thymine base pair is studied in section 3.4 using the BNL range-separated functional.<sup>43,44</sup>

## 2. METHODOLOGY

**2.1. Overview of Real-Time TDDFT.** Time-dependent density functional theory casts the time-dependent Schrödinger equation into a fictitious system of noninteracting electrons that satisfy the effective single particle time-dependent Kohn–Sham (TDKS) equations with an effective potential  $v_{\text{KS}}(\mathbf{r}, t)$  uniquely described by the time-dependent charge density  $\rho(\mathbf{r}, t)$ ,<sup>1</sup> which in atomic units is

$$\begin{aligned} i \frac{\partial \psi_i(\mathbf{r}, t)}{\partial t} &= \left[ -\frac{1}{2} \nabla^2 + v_{\text{KS}}[\rho](\mathbf{r}, t) \right] \psi_i(t) \\ &= \left[ -\frac{1}{2} \nabla^2 + v_{\text{ext}}(\mathbf{r}, t) + v_{\text{H}}(\mathbf{r}, t) + v_{\text{XC}}[\rho](\mathbf{r}, t) \right] \psi_i(t) \end{aligned} \quad (1)$$

Here, the charge density is the sum over all orbitals

$$\rho(\mathbf{r}, t) = \sum_i^{\text{occ}} |\psi_i(\mathbf{r}, t)|^2 \quad (2)$$

and  $v_{\text{ext}}(\mathbf{r}, t)$  contains the nuclear–electron and applied field potentials and  $v_{\text{H}}(\mathbf{r}, t)$  is the Hartree (electron–electron) mean-field potential. Note that all potentials are explicit functions of time. Moreover, the exchange–correlation potential  $v_{\text{XC}}[\rho](\mathbf{r}, t)$  is non-local in both space and time and is formally a functional of the initial wave functions and the entire history of the charge density  $\rho(\mathbf{r}, t)$ . However, all practical implementations use the adiabatic

approximation, which assumes locality in time (see discussion by Baer<sup>45</sup>). Real-time TDDFT involves explicitly propagating the coupled one-particle KS wave functions via eq 1. This is in contrast to the traditional linear-response approach, which is not actually a time-resolved method but instead solves eq 1 in the frequency domain for the excitation energies of a system subject to a small perturbation;<sup>3</sup> there are also real-time linear-response TDDFT approaches.<sup>46,47</sup>

In practical applications, the KS molecular orbitals are either solved in real space (e.g., finite element approaches) or expanded in a set of basis functions. In the case of an orthogonal basis (e.g., plane waves), time evolution consists of propagating the time-dependent coefficients of each of the mutually orthogonal basis functions. Localized basis functions, on the other hand, offer a good compromise between speed and flexibility, and in the case of a Gaussian basis set, they offer the added ability to use hybrid nonlocal exchange–correlation functionals in a seamless manner. In a Gaussian basis, it is most natural to use the single particle reduced density matrix

$$\mathbf{P}'_{\mu\nu} = \sum_i^{N_{\text{MO}}} \mathbf{C}_{\mu i}^*(t) \mathbf{C}_{i\nu}(t) \quad (3)$$

where we have introduced the time-dependent molecular orbital coefficient matrix  $\mathbf{C}(t)$ , which describes the occupations of the molecular orbitals:

$$\psi_i(\mathbf{r}, t) = \sum_{\mu=1}^{N_{\text{AO}}} \mathbf{C}_{\mu i}(t) \phi_{\mu}(\mathbf{r}) \quad (4)$$

where  $\{\phi(\mathbf{r})\}$  are the atomic orbitals,  $N_{\text{AO}}$  is the number of atomic orbitals, and  $N_{\text{MO}}$  is the number of molecular orbitals. From here on, we use primes to denote matrices in the molecular orbital (MO) basis and no primes to denote matrices in the atomic orbital (AO) basis. In the MO (orthonormal) basis, the time evolution of the density matrix is governed by the von Neumann equation

$$i \frac{\partial \mathbf{P}'}{\partial t} = [\mathbf{F}'(t), \mathbf{P}'(t)] \quad (5)$$

where  $\mathbf{F}'(t)$  is the time-dependent Fock matrix in the MO basis, which depends on the density matrix at that time. Evolving the system in time reduces to computing the Fock matrix and stepping  $\mathbf{P}'(t)$  forward using eq 5. For large systems with diffuse basis sets, linear dependencies in the basis become unavoidable; see Appendix A for a detailed discussion on AO↔MO transformations and how to deal with linear dependencies in RT-TDDFT.

Unlike ground state DFT calculations where the density matrix and Fock matrix are purely real (at least in the case of a real basis set like Gaussians), both become complex quantities in real time due to the  $i$  in eq 5. Moreover, whereas they are symmetric in the ground state, they must remain Hermitian under time propagation, with the additional constraint that the density matrix remains idempotent and trace invariant ( $\mathbf{P}'\mathbf{P}' = \mathbf{P}'$ ,  $\text{Tr}[\mathbf{P}'] = N_e$ ), where  $N_e$  is the total number of electrons in the system.

This approach for evolving the density matrix in time is intuitive and easy to implement with a variety of time propagators (see section 2.3). Moreover, it can be readily extended to use matrix and current functionals, and phenomenological damping can be introduced via the off-diagonal elements of  $\mathbf{P}'(t)$  or through friction functionals.<sup>48</sup> The dominant computational

burden is in computing the Fock matrix  $\mathbf{F}'(t)$  at every time step, which is outlined in the following section.

**2.2. Time-Dependent Fock Matrix.** The proper choice of exchange-correlation functional is critical, as the inclusion of nonlocal exchange has been shown to be essential in a broad range of cases.<sup>49–51</sup> LR-TDDFT with global hybrid functionals (e.g., B3LYP, PBE0, and others) has been highly successful in predicting excitation energies for a range of systems.<sup>4,52</sup> More recently, range-separated functionals have been shown to capture charge transfer states successfully.<sup>44,53–56</sup> As such, we consider a composite time-dependent complex Fock matrix, which in general contains a blend of DFT exchange-correlation and Hartree–Fock exchange. This can be written in a general way as follows:

$$\mathbf{F}_{\mu\nu}[\mathbf{P}(t)] = \mathbf{H}_{\mu\nu}^{\text{core}} + \mathbf{G}_{\mu\nu}^J[\mathbf{P}(t)] + \alpha \mathbf{G}_{\mu\nu}^K[\mathbf{P}(t)] + \beta \mathbf{G}_{\mu\nu}^{\text{X-DFT}}[\rho(\mathbf{r}, t)] + \gamma \mathbf{G}_{\mu\nu}^{\text{C-DFT}}[\rho(\mathbf{r}, t)] + \mathbf{V}^{\text{app}}(t) \quad (6)$$

where  $\mu$  and  $\nu$  index the atomic orbitals. Here,  $\mathbf{H}_{\mu\nu}^{\text{core}}$  is the time-independent one-electron part,  $\mathbf{G}_{\mu\nu}^J(t)$  is two-electron Coulomb interaction between the electrons,  $\mathbf{G}_{\mu\nu}^K(t)$  is the two-electron exact exchange,  $\mathbf{G}_{\mu\nu}^{\text{X-DFT}}(t)$  is the DFT exchange part, and  $\mathbf{G}_{\mu\nu}^{\text{C-DFT}}$  is the DFT correlation. The  $\alpha$ ,  $\beta$ , and  $\gamma$  coefficients quantify the mixing of DFT and HF (exact exchange), e.g.,  $\alpha = 1, \beta = \gamma = 0$  for pure HF;  $\alpha = 0, \beta = \gamma = 1$  yields for DFT; and intermediate values for global hybrid functionals.  $\mathbf{V}^{\text{app}}(t)$  includes any external perturbation to the system, such as an applied electric field.

The Coulomb and DFT exchange-correlation contributions are all purely real symmetric matrices that depend only on the real part of the density matrix. The exact exchange matrix  $\mathbf{G}_{\mu\nu}^K(t)$ , however, is complex Hermitian and depends on both the real and imaginary parts of  $\mathbf{P}(t)$ ; see Appendix B for a derivation and discussion of these symmetries. As a consequence, the imaginary part of  $\mathbf{P}(t)$  only enters into the Fock matrix if there is exact exchange (i.e., either pure Hartree–Fock or hybrid functionals), and despite the complex phase introduced into the density matrix via eq 5, the Fock matrix remains purely real in pure DFT calculations.

**2.3. Magnus Propagator.** The final component of the real-time scheme involves integrating eq 5 to get the time-dependent density matrix. Nonsymplectic integrators, such as Euler or Runge–Kutta methods, are unsuitable for large scale simulations as they become increasingly unstable with increased simulation size and require a very small time step to maintain the idempotency constraint of the density matrix. A better choice for von Neumann dynamics is the Magnus expansion, which steps  $\mathbf{P}'$  forward in time using a unitary propagator which conserves the idempotency. We briefly summarize the method below, without derivation. For a general overview of time propagation schemes, see the review by Kosloff.<sup>57</sup> For additional details concerning propagators for the time-dependent Kohn–Sham equations, see refs 58 and 36 and also the excellent discussion by Castro and co-workers.<sup>59</sup>

The exact unitary propagator for eq 5 is given by

$$\mathbf{U}(t + \Delta t, t) = T \exp\left\{-i \int_t^{t+\Delta t} \mathbf{F}'(\tau) d\tau\right\} \quad (7)$$

such that

$$\mathbf{P}'(t + \Delta t) = \mathbf{U}(t + \Delta t, t) \mathbf{P}'(t) \mathbf{U}^\dagger(t + \Delta t, t) \quad (8)$$

where  $T$  is the time-ordering operator which orders operators from those associated with later times to earlier times. The

explicit time dependence of  $\mathbf{F}'(t)$  makes it impossible to evaluate this propagator directly. Instead, a convenient solution to eq 7 is given by a Magnus expansion<sup>60</sup>

$$T \exp\left\{-i \int_t^{t+\Delta t} \mathbf{F}'(\tau) d\tau\right\} = e^{\Omega_1 + \Omega_2 + \dots} \quad (9)$$

where the  $\{\Omega_i\}$  are a series of nested commutator integrals:

$$\Omega_1(t + \Delta t, t) = -i \int_t^{t+\Delta t} \mathbf{F}'(\tau) d\tau \quad (10)$$

$$\Omega_2(t + \Delta t, t) = -i \int_t^{t+\Delta t} d\tau_1 \int_t^{\tau_1} [\mathbf{F}'(\tau_2), \mathbf{F}'(\tau_2)] \quad (11)$$

$$\vdots \quad (12)$$

The resulting approximation is valid to order  $\Delta t^{2M}$ , where  $M$  is the number of Magnus terms. The integrals in eq 10 can be evaluated using quadrature. For example, for  $M = 1$ , we have

$$\mathbf{U}(t + \Delta t, t) \approx e^{\Omega_1} \quad (13)$$

$$\Omega_1 \approx -i \mathbf{F}'(t + \Delta t/2) \quad (14)$$

The results presented here all used a  $M = 1$  Magnus expansion; increasing to  $M = 2$  would allow larger time steps, at the cost of more Fock builds per time step.

The main difficulty in using a Magnus scheme arises from the fact that the propagation (e.g., eq 14) requires knowledge of the Fock matrix at a future time, which is unknown. In the case of a second order ( $M = 1$ ) Magnus propagator, the obvious solution is to form a guess for  $\mathbf{F}'(t + \Delta t/2)$  from a linear extrapolation of  $\mathbf{F}'$  at previous times. Unfortunately, crude predictors such as this inevitably fail for larger time steps. The most accurate method is to extrapolate  $\mathbf{F}'$ , propagate  $\mathbf{P}'$  forward, interpolate to find a better  $\mathbf{F}'$ , and repeat until converged. This approach is costly, however, as you must rebuild the Fock matrix every convergence step. Instead, we adopted a two step predictor–corrector scheme proposed by Van Voorhis and co-workers,<sup>27</sup> whereby you predict  $\mathbf{F}'(t + \Delta t/4)$  by linear extrapolation from previous values and use this to step  $\mathbf{P}'$  forward by  $\Delta t/2$  using eq 7. Overall, the predictor–corrector scheme was found to be sufficiently accurate and stable for a wide variety of systems. Predictor schemes such as this, however, fail to conserve the time-reversibility of eq 5. One alternate approach is the modified midpoint unitary transformation (MMUT) method developed by Li and co-workers;<sup>11</sup> the MMUT approach will be implemented in the future.

Finally, the exponentiation of the  $\Omega$  matrices can be performed using a range of methods such as diagonalization, power series, Lanczos, etc. Note, however, that  $\mathbf{U}^\dagger = \mathbf{U}^{-1}$  (unitary), so eq 7 is of the form

$$\mathbf{P}'(t + \Delta t) = e^{\mathbf{W}} \mathbf{P}'(t) e^{-\mathbf{W}} \quad (15)$$

where  $\mathbf{W}(t + \Delta t, t) = \Omega_1(t + \Delta t, t) + \Omega_2(t + \Delta t, t) + \dots$ . Thus, we can apply the Baker–Campbell–Hausdorff (BCH) formula

$$\begin{aligned} \mathbf{P}'(t + \Delta t) = & \mathbf{P}' + \frac{1}{1!} [\mathbf{W}, \mathbf{P}'(t)] + \frac{1}{2!} [\mathbf{W}, [\mathbf{W}, \mathbf{P}'(t)]] \\ & + \frac{1}{3!} [\mathbf{W}, [\mathbf{W}, [\mathbf{W}, \mathbf{P}'(t)]]] + \dots \end{aligned} \quad (16)$$



For clarity, we have dropped the explicit time dependence of the  $W(t+\Delta t, t)$  matrix. The BCH expansion converges much better than a simple power series expansion, and the primary advantage of the BCH expansion over diagonalization is that eq 16 consists entirely of matrix multiplications, which are operations that parallelize extremely well. Although diagonalization formally scales as  $O(N^3)$  and is thus more efficient than a series of matrix multiplications (each of which takes exactly  $N^3$  effort in the absence of sparsity), in practical applications, diagonalization is hard to parallelize well. Due to inefficiencies, diagonalization becomes a serious bottleneck in quantum chemistry simulations run on more than a few hundred processors, and thus for large-scale simulations, diagonalization-free approaches are better suited (see ref 61 and references therein). In practice, it usually took on the order of tens of terms to converge the BCH expansion to  $10^{-8}$  accuracy.

**2.4. Computational Considerations.** Accurate electron dynamics simulations of realistic systems can easily involve thousands of electrons and basis functions, propagated for long times. Clearly, an efficient implementation is necessary to make such simulations feasible. Since the vast majority of the computational work comes from building the Fock matrix at each time step, effort should be taken to either increase  $\Delta t$  or speed up construction of the Fock matrix.

Higher order Magnus propagators allow for larger time steps, for example, but require added Fock builds at each step; in practice, however, this is a system-specific trade-off. On the other hand, the Fock matrix construction can be sped up by using smaller basis sets or pure DFT functionals (e.g., ALDA), in conjunction with approaches such as charge density fitting.<sup>62</sup> Semiempirical Hamiltonians are also an alternative<sup>12</sup> but need to be properly parametrized and carefully validated.

The von Neumann dynamics approach as formulated is straightforward to implement in any quantum chemistry suite, as it can be built on fundamental routines. Constructing the time-dependent Fock matrix (eq 6) is akin to the building the ground state  $F$  in standard SCF (self-consistent field) schemes, save for the imaginary part due to exact exchange. Provided parallelization bottlenecks like diagonalization are avoided (as in the BCH exponentiation approach), RT-TDDFT will scale as well as standard Gaussian orbital-based SCF DFT with no loss of generality. We have implemented this approach, in NWChem which allows us to take advantage of the efficient parallelization capabilities offered by the code. This in turn allows us to tackle large systems with a high level of accuracy.

### 3. RESULTS

In this section, we first validate the real-time TDDFT approach against linear response TDDFT for series of small molecules, then move on to study the response of two chromophores to weak and strong perturbations, and finally study charge transfer across a DNA base pair using a long-range corrected, or range-separated, functional. Throughout, we mostly use atomic units (au), but for convenience we also present values in more customary units: 1 au length = 0.5292 Å; 1 au energy = 27.21 eV; 1 au time = 0.02419 fs; 1 au dipole moment = 2.542 D; 1 au electric field = 514.2 V/nm. Unless noted otherwise, all basis sets used in this study were obtained from the EMSL Basis Set Exchange.<sup>63</sup>

**3.1. Validation on Small Molecules.** To validate that the RT-TDDFT approach correctly reduces to linear response in the

small perturbation limit, we studied the lowest excitation energies of various molecules and compared the results to standard LR-TDDFT and experimental results. An optical absorption spectrum can be obtained from a real-time simulation via Fourier transform of the time-dependent dipole moment resulting from a small  $\delta$ -function-like electric field “kick”. Starting from the ground state, we perturb the system with a narrow, transient, linearly polarized uniform Gaussian electric field:

$$E(t) = \kappa \exp[-(t - t_0)^2/2w^2] \hat{d} \quad (17)$$

where  $t_0$  is the center of pulse,  $w$  is the pulse width (typically a few time steps), which has dimensions of time,  $\hat{d} = \hat{x}, \hat{y}, \hat{z}$  is the polarization of the pulse, and  $\kappa$  is the maximum field strength (dimensions of electric field). Note that the total energy added is therefore dependent on the time step  $\Delta t$  and the pulse width  $w$ ; alternatively a normalized pulse can be used. The applied field excites the system through a dipole coupling term added to the Fock matrix (in the AO basis)

$$V_{\mu\nu}^{\text{app}}(t) = -D_{\mu\nu} \cdot E(t) \quad (18)$$

where  $D$  is the transition dipole tensor of the system, e.g.,

$$D_{\mu\nu}^x = \int \phi_{\mu}^*(\mathbf{r}) x \phi_{\nu}(\mathbf{r}) d\mathbf{r} \quad (19)$$

A Gaussian-type electric field was chosen instead of a  $\delta$ -function to avoid introducing nonphysical artifacts or instabilities due to a sudden change in potential. Despite the finite width, the pulse essentially excites all electronic frequencies simultaneously, save perhaps very high frequencies. The system is allowed to evolve in time, and the dipole moment is computed in the AO basis according to

$$\mu(t) = \text{Tr}[D P(t)] \quad (20)$$

Likewise, the time-dependent occupation of the  $k$ th molecular orbital is computed by projecting the density matrix onto the ground state orbitals

$$n_k(t) = C_k'^{\dagger} P'(t) C_k' \quad (21)$$

where  $C_k'$  is the  $k$ th eigenvector of the ground state Fock matrix. To get the absorption spectrum from RT-TDDFT, a simulation is performed for each polarization of kick (symmetries in the system may alleviate this need), and the complex polarizability tensor is constructed from the Fourier transforms of the dipole signals

$$\alpha_{d,j}(\omega) = \frac{1}{\kappa} \tilde{\mu}_{d,j}(\omega) \quad (22)$$

where  $d$  is the index for the kick direction and  $j$  is the index for the measurement direction. The absorption cross-section tensor is obtained from  $\alpha(\omega)$  via

$$\sigma(\omega) = \frac{4\pi\omega}{c} \text{Im}[\alpha(\omega)] \quad (23)$$

and finally the dipole strength function (absorption spectrum) is

$$S(\omega) = \frac{1}{3} \text{Tr}[\sigma(\omega)] \quad (24)$$

Figure 1 shows real-time data for benzene described using the 6-31G\* basis set, subjected to a small  $x$  kick with  $\kappa = 2 \times 10^{-5}$  au = 10 mV/nm,  $w = 0.2$  au =  $4.8 \times 10^{-3}$  fs, and  $t_0 = 3$  au = 0.07 fs. Before perturbing the system, the nuclear geometry was optimized

## Real-time results for benzene

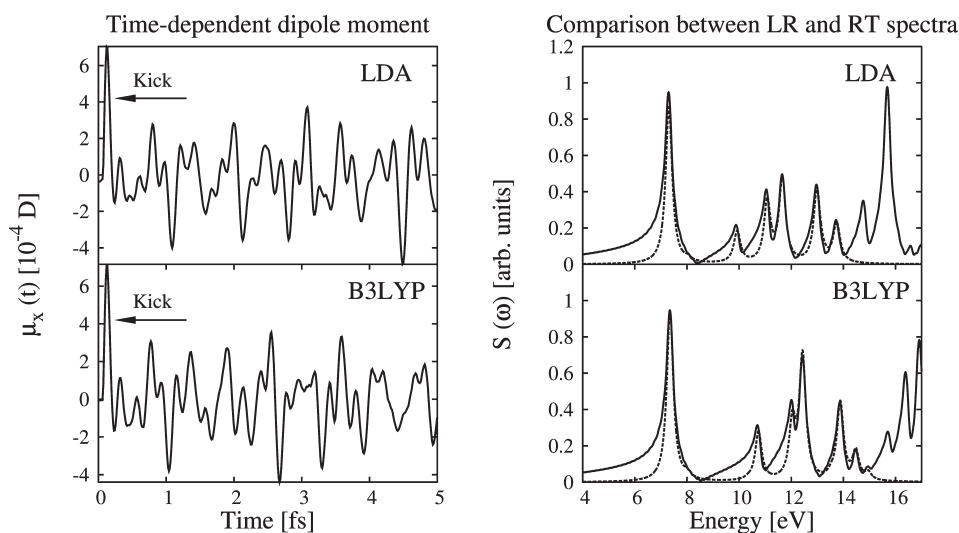


**Figure 1.** Real-time (RT) results for benzene in the perturbation limit, described using the 6-31G\* basis and LDA (top) and B3LYP (bottom) functionals. The left panel shows the  $x$  dipole moment after a narrow Gaussian electric field kick. The resulting absorption spectra are shown on the right (solid lines), with the corresponding linear-response (LR) spectra shown for comparison (fine dashed lines). The peaks were artificially broadened and normalized (see text).

using the same basis and functional, and the ground state density converged via standard DFT. The narrow electric field pulse simultaneously excites all electronic modes, and the full dipole response (left panel) shows essentially dipolar oscillations composed of multiple frequencies.

A time step of  $\Delta t = 0.5$  au = 0.012 fs was used, and the system was evolved for 1000 au = 24 fs. Two functionals were used, LDA and B3LYP, which yielded qualitatively similar results. For speed, in the LDA case, the Coulomb part of the Fock matrix was evaluated using charge density fitting instead of the explicit two-electron integrals;<sup>62</sup> this significantly reduced the computational cost. We checked that the charge density fitting approach yielded very similar results to explicit calculation of the Coulomb integrals. As an additional check, we confirmed that after the pulse had passed, the total system energy remained constant over time. The resulting absorption spectra are shown in the right panel, where the peaks have been broadened by artificially damping the time signal by  $e^{-t/\tau}$ ,  $\tau = 250$  au = 6 fs before taking the Fourier transform.

To validate these results, the corresponding linear response TDDFT spectra were compared with those obtained using the linear response TDDFT module in NWChem. The dashed lines show the LR spectrum, artificially broadened with Lorentzians of width 0.01 au = 0.3 eV. Additionally, both RT and LR spectra were normalized for clarity. The two spectra are essentially identical. For each of the finite LR signals (100 total roots computed for each simulation yielding six signals with appreciable oscillator strength), the RT signal agrees perfectly. Since the RT result effectively samples all excitations, rather than a finite number of roots as in LR, the RT spectra contain higher frequency signals beyond those computed in the LR simulation.

As an aside, the spectral resolution of the RT approach is limited by the time step; i.e., if a molecule has a spectral bandwidth of  $\omega_{\max}$  the maximum time step is  $\Delta t_{\max} = \pi/\omega_{\max}$ . As an extreme example, to resolve the spectrum of a molecule with a maximum excitation frequency of 2 au (54 eV), one requires a time step of  $\Delta t = 1.57$  au = 0.034 fs, or smaller. In

practice, however, the time step is limited by the stability of the propagator (e.g. Magnus) rather than the bandwidth.

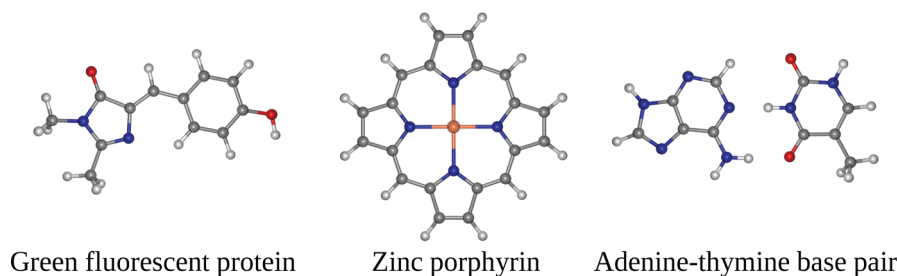
As further validation, a similar analysis was conducted for a range of small molecules, basis sets, and functionals, using the same kick parameters as described above. As before, geometry optimizations and convergence of the ground state densities were performed using the same basis and functionals as each of the real-time simulations. Table 1 shows a comparison between the linear-response, real-time, and gas-phase experimental lowest excitation energies for dihydrogen, methane, carbon monoxide, and benzene. Overall, there is excellent agreement between the linear-response (LR) and real-time (RT) values, as well as with experimental results. At worst, the RT energy deviated from the LR result by  $\sim 1\%$  and from the experimental one by  $\sim 10\%$ , with agreement generally improving with size of the basis set.

We note that a RT-TDDFT kick-type simulation yields the full electronic spectrum, up to the cutoff energy due to the finite time step. Thus, unlike a LR-TDDFT approach which requires a large number of roots or a windowed solver to compute higher energy transitions, a kick approach yields all roots in one single simulation, or at most three simulations ( $x, y, z$  kicks) in the absence of symmetries. Indeed, if one is interested in computing many excitation energies for a very large system, the RT approach is actually more efficient than a LR approach, which requires  $\approx O(N^4)$  effort for each root.<sup>64</sup> The one caveat is that, as formulated, a RT-TDDFT simulation can only probe excitations with a nonzero oscillator strength and thus cannot be effectively used to study “dark” excitations, which are typically measured experimentally via emission.

**3.2. Linear and Nonlinear Excitation of Green Fluorescent Protein.** Green fluorescent protein (GFP), which is responsible for the bioluminescence of some species of jellyfish, is nearly ubiquitous in biotechnology, with technological applications ranging from visualizing tagged proteins using fluorescence microscopy to developing transgenic fluorescent organisms.<sup>65</sup> Depending on the variant, GFP absorbs light in the blue or

**Table 1.** Comparison of Real-Time (RT) TDDFT, Linear Response (LR) TDDFT, and Experimental Lowest Excitation Energies (in eV) for a Selection of Molecules, Basis Sets, and Exchange-Correlation Functionals

	6-311G/LDA		6-311G/B3LYP		cc-pVTZ/LDA		cc-pVTZ/B3LYP		expt
	LR	RT	LR	RT	LR	RT	LR	RT	
H <sub>2</sub>	12.52	12.49	13.09	13.12	12.32	12.31	12.88	12.90	11.19
CH <sub>4</sub>	10.67	10.67	11.10	11.13	10.29	10.29	10.72	10.75	9.70
CO	8.00	8.03	8.16	8.22	8.29	8.28	8.52	8.55	8.55
C <sub>6</sub> H <sub>6</sub>	7.31	7.35	7.35	7.36	7.09	7.10	7.15	7.18	6.90

**Figure 2.** Structures of the molecules studied.

ultraviolet and fluoresces in the green. The actual GFP chromophore, which is a small molecule embedded in the larger overall protein, has a strong absorption due to a single excitation, which makes it an ideal candidate for TDDFT studies. The particular chromophore variant we studied (see Figure 2) has an intense experimental absorption at 3.51 eV, which corresponds to 354 nm light.<sup>66</sup> In the weak-field regime, linear response TDDFT calculations (3.32 eV B3LYP/POL1) agree well with both coupled cluster (3.60 eV CR-EOMCCSD(T)/POL1) and the experimental values for the absorption (see ref 67). Modeling the full response of GFP to strong fields beyond the weak perturbation limit, however, requires a real-time approach, and in this section, we use RT-TDDFT to study the nonlinear excitation of GFP subject to a range of perturbations.

To explore the nonlinear absorption properties, we subjected the GFP chromophore to a series of kicks (as in section 3.1) with field maximum  $\kappa$  ranging from  $8 \times 10^{-4}$  au = 0.41 V/nm (weak perturbation) to 0.24 au = 123 V/nm (strong perturbation). These narrow pulses ( $w = 4.8 \times 10^{-3}$  fs) are nonphysical fields that simultaneously excite all electronic modes; this results in a nonphysical dipole moment which is a convolution of all excitations. Correspondingly, these simulations describe the immediate absorption properties of the molecule (i.e., how the light is absorbed and excites the density), and although the larger values of  $\kappa$  correspond to extremely strong electric fields, these simulations do not capture photoionization, which is difficult to describe using TDDFT in an atom-centered basis. Estimating ionization probabilities over a range of frequencies from a single kick-type nonphysical excitation is not straightforward, as the energy is distributed among all electrons in the system (i.e., core to valence); this will be quantified in future studies.

To ensure that there were sufficient basis functions to capture the diffuse excited states for the highly excited cases, we used the POL1 basis set.<sup>68</sup> In total, there were 114 electrons and 492 basis functions. To rule out unphysical confinement of the charge density due to the finite basis, we also tried using the smaller

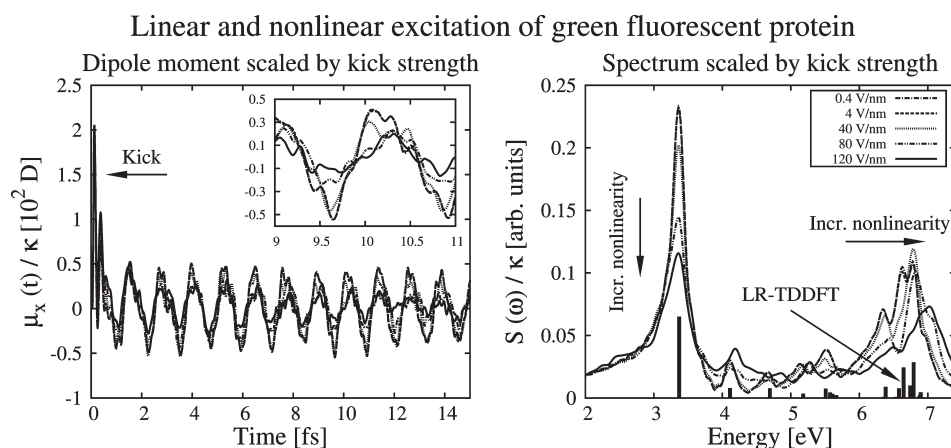
6-31G\* basis set; the results were essentially identical. We used the B3LYP exchange-correlation functional for this study. To ensure we start at an energy minimum, we used the same basis set and functional for geometry optimization and ground state density convergence before starting the time-dependent simulation. The density matrix was propagated for 1300 au = 31 fs with a time step of  $\Delta t = 0.1$  au = 0.0024 fs.

Figure 3 shows the dipole moment and absorption spectrum (artificially broadened via damping by  $e^{-t/\tau}$ ;  $\tau = 400$  au = 9.7 fs) for this range of perturbations. For illustrative purposes, relative values are presented—the dipole moment is scaled by the kick height such that any results in the weak excitation regime will be identical. Alternatively, in the linear response regime, if you double the kick, the dipole moment will double; this does not hold true in the strong excitation regime, which provides a simple graphical indicator of nonlinearity.

Once the perturbation is strong enough (i.e.,  $\kappa \gtrsim 40$  V/nm in Figure 3), two interesting effects emerge. First, the scaled responses (heights of the dipole moment and absorption peaks) decrease in magnitude; this is a saturation effect. Physically, once one goes beyond linear response, the highly excited molecule cannot absorb subsequent radiation, and the absorption, which is due to a single excitation, saturates. Nonlinear saturation effects like this, which are neglected by linear response, are critical for realistic modeling of spectroscopy under intense fields and transport in nanosystems where LR transport calculations tend to drastically overestimate certain effects.

Second, in the nonlinear regime, higher frequency signals begin to dominate. The inset in the left panel of Figure 3 shows how in the strong perturbation regime the time signal is no longer dominated by the main slow (low frequency) excitation, but instead by higher frequency modes. The corresponding spectrum shows how the absorption is likewise spread out over a wider range of frequencies. Moreover, in the nonlinear regime, the secondary absorption around 6.8 eV is increasingly blue-shifted with stronger fields.





**Figure 3.** The dipole moment (left) and spectrum (right) of the green fluorescent protein chromophore subjected to a series of kicks ranging from the weak to the highly nonlinear regimes. For comparison, the values are scaled by the kick strength and the spectrum plot also shows the corresponding linear response TDDFT roots. In the nonlinear regime ( $\kappa \gtrsim 40$  V/nm), the molecule's excitation is saturated, and higher frequency signal modes begin to dominate the time-resolved dipole moment. The strength of the main absorption in the spectrum decreases with nonlinearity, and the secondary higher energy absorption is increasingly blue-shifted.

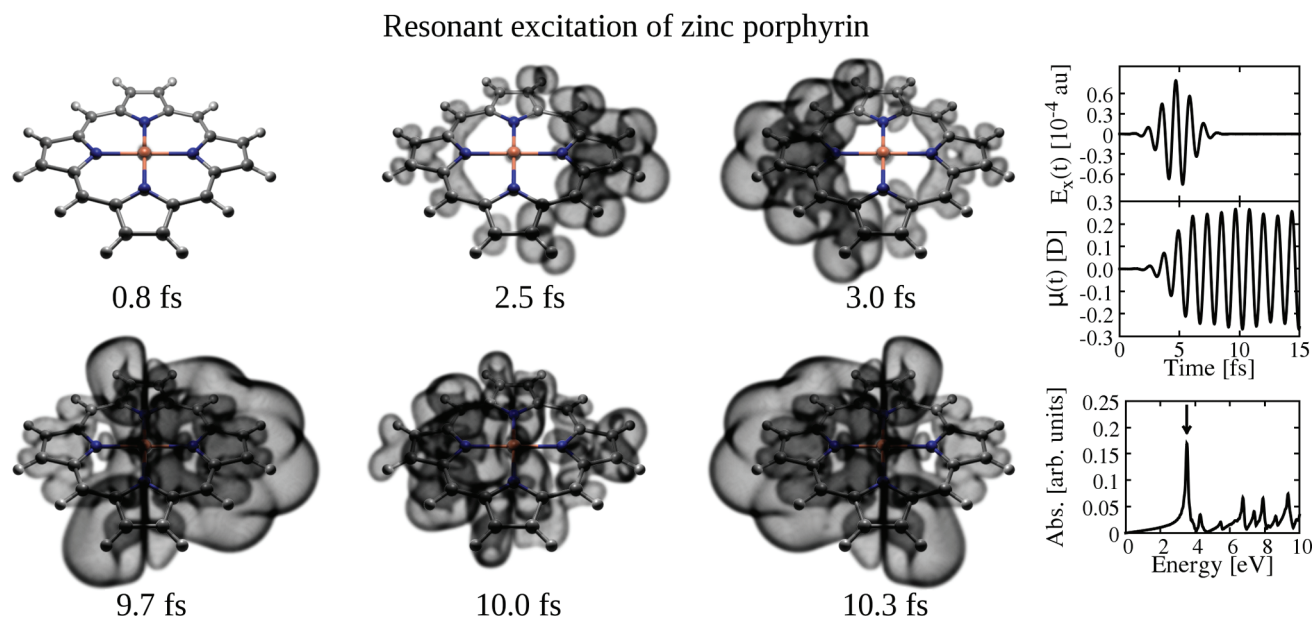


**Figure 4.** Isosurface snapshots of the difference between the excited and ground state charge densities,  $\rho(\mathbf{r},t) - \rho(\mathbf{r},0) = 7 \times 10^{-7} \text{ \AA}^{-3}$ , for zinc porphyrin described using B3LYP and 6-31G\* for H, C, and N and the Stuttgart RSC 1997 effective core potential for Zn. The system was excited at its resonance of 3.53 eV (see bottom inset spectrum) with a transient  $x$ -polarized laser pulse (top inset), resulting in charge oscillation back and forth along the molecule's conjugated  $\pi$  backbone, with each complete oscillation taking  $\sim 1.2$  fs. The charge density was plotted using Blender.<sup>75</sup>

A simple physical interpretation is that the highly displaced charge density experiences a nonlinear restoring force which is stronger than in the linear regime, just like a highly displaced spring.

**3.3. Resonant Excitation of Zinc Porphyrin.** Porphyrin forms the structural basis for the various chlorophyll molecules and has been exploited as the functional unit in light harvesting systems.<sup>69,70</sup> The absorption properties of zinc and free-base porphyrin have been studied extensively using LR-TDDFT and coupled cluster theory,<sup>54,67,71</sup> but from a photovoltaic device point of view, the mechanism of charge injection (i.e., from the light harvesting porphyrin into a nearby substrate) has many unanswered questions. RT-TDDFT is an excellent tool to probe these charge dynamics in real time and real space.

As a first step in this direction, we model the response of zinc porphyrin (Figure 2) to a transient laser pulse tuned to its strongest absorption. We used B3LYP for the exchange correlation; for the basis set, we used 6-31G\* for the hydrogen, carbon, and nitrogen atoms and the Stuttgart RSC 1997 effective core potential (ECP) for the zinc center, which replaces 10 of the Zn electrons. Since optical absorption does not typically involve core electrons, ECPs offer a simple way to boost the speed of real-time calculations without a loss of accuracy; we confirmed that the use of an ECP in this case did not alter the results. The total propagation time was 1500 au = 36 fs with a time step of  $\Delta t = 0.1$  au = 0.0024 fs, which was chosen to ensure a smooth density animation rather than being limited by the propagator.

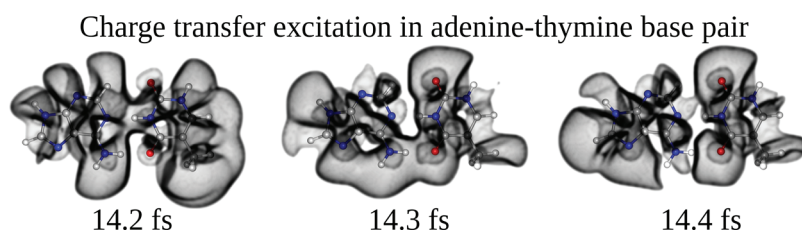


**Figure 5.** Snapshots of  $\rho(\mathbf{r},t) - \rho(\mathbf{r},0) = 10^{-7} \text{ \AA}^{-3}$  for the adenine (A, left molecule)/thymine (T, right molecule) base pair excited at the 6.36 eV resonance, corresponding to an intermolecular charge transfer state. The snapshots correspond to times long after the transient laser pulse has passed, leaving the system in an excited state. Initially, both molecules are polarized in the  $+x$  direction, and there is an excess of charge on T. Next, charge is transferred  $A \leftarrow T$  via the  $\text{NH}_2 \cdots \text{O}=\text{C}$  bridge, resulting in a net  $-x$  overall polarization and excess charge on A. The overall charge transfer happens in approximately 0.3 fs. The charge density was plotted using Blender.<sup>75</sup>

The enveloped monochromatic laser pulse took the form

$$E_x(t) = k \exp[-(t - t_0)^2/2w^2] \cos(\omega_0 t), \quad (25)$$

$$E_y = E_z = 0$$

The frequency of the pulse was taken to be  $\omega_0 = 0.1296 \text{ au} = 3.53 \text{ eV}$ , and the Gaussian had a half-width of  $w = 50 \text{ au} = 1.2 \text{ fs}$ . The maximum field strength was  $\kappa = 8.0 \times 10^{-5} \text{ au} = 41 \text{ mV/nm}$ , which is within the linear response regime. The ZnP resonance frequency was determined from a kick-type simulation (see eq 17 in section 3.1) and artificially broadened. The resulting spectrum is shown in the bottom inset of Figure 4, with an arrow denoting the laser pulse frequency. The top inset shows the profile for the homogeneous  $x$ -polarized monochromatic electric field pulse used in this resonant excitation (overall the pulse lasts approximately 7 fs). The middle plot shows the resulting dipole moment which is essentially monochromatic, and as there is no damping in the system, the oscillation continues indefinitely.

The six panels in Figure 4 show snapshots of the deviation of the charge density from the ground state,  $\rho(\mathbf{r},t) - \rho(\mathbf{r},0)$  during and after resonant illumination. The snapshots show the positive  $7 \times 10^{-7} \text{ \AA}^{-3}$  isosurface, i.e., the smooth surface where  $\rho(\mathbf{r},t) - \rho(\mathbf{r},0) = 7 \times 10^{-7} \text{ \AA}^{-3}$ ; the corresponding negative deviation was omitted for clarity. The top three slices depict the response of the charge density while being driven by the laser pulse.  $\rho(\mathbf{r},t)$  starts essentially in the ground state (first slice). The second slice occurs just at the first significant peak in the dipole moment, which occurs just after the peak in the driving field, as it takes time for the density to respond. Here, the extra charge density is beginning to populate the space above and below the carbon backbone on the  $+x$  (right) side of the molecule, which corresponds to a  $\pi \rightarrow \pi^*$  transition. The third slice, which is the first significant trough in the total dipole moment, demonstrates that the charge density now populates the  $\pi^*$  orbitals on the  $-x$  (left) side of the molecule. The bottom three slices show how the charge density of the excited ZnP molecule evolves after the driving field has passed. The charge density sloshes along the delocalized  $\pi^*$  orbitals from the right to the left, which takes  $\sim 24 \text{ au} = 0.6 \text{ fs}$ , which is in agreement with the time-resolved dipole moment (middle inset).

Using RT-TDDFT to directly visualize the electron dynamics offers insight into the fundamental nature of the excitation, not just concerning which molecular orbitals are at play but also how they are being populated in time, and where in space the charge is concentrated. In Figure 4, not only is the  $\pi \rightarrow \pi^*$  transition obviously visible, but additionally, as expected, there is a clear buildup of charge at the  $x$  end of the molecule during the oscillations. It is easy to see that bonding a porphyrin to a

substrate will then allow the excited charge density, which has high momentum, to hop from the end of the molecule to the surface in an ultrafast injection process; future RT-TDDFT studies will explore this effect further.

### 3.4. Long-Range Charge Transfer in DNA Base-Pair Fragments.

As a final example, we demonstrate how long-range corrected functionals can be used in a RT-TDDFT framework to correctly capture charge transfer excitations. The charge transfer between adenine (A) and thymine (T) is a classic example where local exchange-correlation functionals (LDA) and even global hybrids (e.g. B3LYP) underestimate the energy of the  $A\pi \rightarrow T\pi^*$  intermolecular transition, to the point that they incorrectly predict it will be the lowest excitation.<sup>50,55</sup> The source of this error is the incorrect asymptotic behavior of the exchange term, which should go as  $r_{12}^{-1}$  but goes as  $0.2r_{12}^{-1}$  in B3LYP, for example. Recently developed long-range corrected functionals have shown great promise in addressing this shortcoming.<sup>44,53–56,72</sup> These functionals split the exchange into a short-range part and a long-range piece which converges to the correct Hartree–Fock asymptote:

$$\frac{1}{r_{12}} = \frac{1 - \text{erf}(\mu r_{12})}{r_{12}} + \frac{\text{erf}(\mu r_{12})}{r_{12}} \quad (26)$$

Here,  $\mu$  is a tuning parameter for partitioning the exchange, where  $\mu \rightarrow 0$  tends to the pure DFT limit and  $\mu \rightarrow \infty$  tends to the pure HF limit.

The real-time response of the A–T pair (see Figure 2) was modeling using the 6-31G\* basis set and the BNL range separated functional<sup>43</sup> with  $\mu = 0.3$ . The Coulomb part of the Fock matrix was computed using charge density fitting with the Ahlrichs Coulomb fitting basis set.<sup>62</sup> The system was excited with a transient laser pulse tuned to the charge transfer excitation in the linear response regime:  $\omega_0 = 0.234 \text{ au} = 6.36 \text{ eV}$ ,  $w = 30 \text{ au} = 0.7 \text{ fs}$ , and  $\kappa = 1.2 \times 10^{-4} \text{ au} = 62 \text{ mV/nm}$  (see eq 25). The resonant frequency was found via kick-type simulation as described previously; it compares well with the value of 6.25 eV from ref 55 computed using LR-TDDFT with BNL ( $\mu = 0.3$ ) and the aug-cc-pVTZ basis set.

Figure 5 shows three snapshots of the  $\rho(\mathbf{r},t) - \rho(\mathbf{r},0) = 10^{-7} \text{ \AA}^{-3}$  density deviation isosurface long after the exciting laser pulse has passed. In the first frame ( $t = 14.2 \text{ fs}$ ), both molecules are polarized in the  $+x$  direction, and there is shared electron density in the central  $\text{N} \cdots \text{H}$  bridge. In the second frame (0.1 fs later), excess charge passes from the thymine molecule through the  $\text{NH}_2 \cdots \text{O}=\text{C}$  bridge, finally resulting in a charge buildup on adenine another 0.1 fs later and a net  $-x$  polarization for both molecules. These simulations show that the complete A $\leftarrow$ T charge transfer process occurs in approximately 0.3 fs. Note that



these dynamics are much faster than the experimentally observed 100 fs decay time for this excitation (likely due to internal conversion to  $n\pi^*$ ).<sup>73</sup>

#### 4. CONCLUSIONS

We have presented Gaussian basis set-based real-time, time-dependent density functional theory simulations using NWChem and have shown that the calculated spectra for a range of small molecules correctly reduce to the linear response TDDFT spectra in the small perturbation limit. Going beyond linear response, we studied the optical response of the green fluorescent chromophore to a series of perturbations of increasing strength. In the strong perturbation regime, the main absorption saturates and the higher energy absorption becomes blue-shifted with increasing field strengths; this has implications for strong field studies of molecules and electron transport in nanosystems. Next, we studied the resonant excitation of the light-harvesting molecule zinc porphyrin. Direct visualization of the charge density in time and space shows that the excitation, which corresponds to a  $\pi \rightarrow \pi^*$  transition, induces delocalized charge oscillations across the carbon backbone, with a buildup of charge near the ends of the molecule. Real-time, real-space studies of this kind offer powerful insight into electron dynamics and are uniquely well-suited to modeling fast electron processes in a variety of devices, such as photovoltaics. Finally, we visualized the adenine  $\pi \rightarrow$  thymine  $\pi^*$  transition, which shows that the charge transfer happens through the oxygen–amine bridge on the order of 0.3 fs. From a computational point of view, the implementation is massively parallel and is scalable with system size; as there is no diagonalization, the main burden is construction of the Fock matrix, which is easily distributed across many processors. Further improvements to the implementation are planned, which will be presented in future publications.

#### ■ APPENDIX A: CANONICAL ORTHOGONALIZATION TRANSFORMS

The real-time TDDFT scheme requires working in both the atomic orbital (AO) and molecular orbital (MO) representations. The propagation is done entirely in the MO basis via the von Neumann equation, eq 5, whereas the Fock matrix is built in the AO basis, eq 6. The time-dependent dipole moment is computed in the AO basis, eq 20, and the time-dependent orbital occupations are computed in the MO basis, eq 21. It is therefore useful to outline how to perform AO  $\leftrightarrow$  MO transformations.

For a given overlap matrix  $S_{\mu\nu} = \langle \phi_\mu | \phi_\nu \rangle$ , there may be linear dependencies in the eigenvectors which necessitates truncating the number of molecular orbitals using canonical orthogonalization. Although not typically a problem in smaller systems, as the system size increases or many diffuse atomic orbitals are used (which is necessary to capture diffuse excited states), linear dependencies become unavoidable. The well-known transformation matrix for converting from the AO to a truncated MO basis is<sup>74</sup>

$$\mathbf{X} = \mathbf{U}\mathbf{s}^{-1/2} \quad (27)$$

where  $\mathbf{U}$  is the matrix with eigenvectors of  $\mathbf{S}$  as columns, and  $\mathbf{s}$  is the diagonal matrix of eigenvalues of  $\mathbf{S}$ . If we have  $N$  atomic orbitals and  $d$  linear dependencies,  $\mathbf{X}$  becomes a rectangular matrix of dimensions  $N \times M$ , where  $M = N - d$  is the number of

molecular orbitals. Converting the Fock matrix from the AO basis to the MO basis is then straightforward:

$$\mathbf{F}' = \mathbf{X}^\dagger \mathbf{F} \mathbf{X} \quad (28)$$

Note that  $\mathbf{F}$  (AO basis) is an  $N \times N$  matrix, whereas  $\mathbf{F}'$  (MO basis) is a smaller  $M \times M$  matrix. Converting the density matrix from the MO to the AO basis is likewise very simple:

$$\mathbf{P} = \mathbf{X} \mathbf{P}' \mathbf{X}^\dagger \quad (29)$$

where, as before,  $\mathbf{P}$  is  $N \times N$  and  $\mathbf{P}'$  is  $M \times M$ . It is slightly more complicated to convert  $\mathbf{P} \rightarrow \mathbf{P}'$ , which is necessary when converting the ground state density matrix, which is computed in the AO basis in an SCF approach, to the MO basis for subsequent von Neumann propagation. Simple inversion of eq 29 is complicated by the fact that  $\mathbf{X}$  is not square and cannot be easily inverted.

The simplest solution is to use left and right inverses. The left inverse of  $\mathbf{X}$  is given by

$$\mathbf{X}_L^{-1} = (\mathbf{X}^\dagger \mathbf{X})^{-1} \mathbf{X}^\dagger \quad (30)$$

while the right inverse of  $\mathbf{X}^\dagger$  is given by

$$(\mathbf{X}^\dagger)_R^{-1} = \mathbf{X} (\mathbf{X}^\dagger \mathbf{X})^{-1} \quad (31)$$

We know these inverses exist because all zero (or near zero) eigenvectors have been removed. From eq 29, we get

$$\mathbf{X}_L^{-1} \mathbf{P} (\mathbf{X}^\dagger)_R^{-1} = \mathbf{P}' \quad (32)$$

which means

$$\mathbf{P}' = (\mathbf{X}^\dagger \mathbf{X})^{-1} \mathbf{X}^\dagger \mathbf{P} \mathbf{X} (\mathbf{X}^\dagger \mathbf{X})^{-1} \quad (33)$$

From eq 27, we know

$$\mathbf{X}^\dagger = \mathbf{s}^{-1/2} \mathbf{U}^\dagger \quad (34)$$

Although  $\mathbf{U}$  is not strictly unitary (as it is not square), we know that  $\mathbf{U}^\dagger \mathbf{U} = \mathbf{I}_m$ , and thus  $(\mathbf{X}^\dagger \mathbf{X})^{-1} = \mathbf{s}$ . The transformation from the density matrix in the AO basis to the MO basis then becomes

$$\mathbf{P}' = \mathbf{s} \mathbf{X}^\dagger \mathbf{P} \mathbf{X} \mathbf{s} \quad (35)$$

which in a more compact form is simply

$$\mathbf{P}' = \mathbf{Y}^\dagger \mathbf{P} \mathbf{Y} \quad (36)$$

where  $\mathbf{Y} \equiv \mathbf{X} \mathbf{s} = \mathbf{U} \mathbf{s}^{1/2}$  is an  $N \times M$  transformation matrix.

#### ■ APPENDIX B: SYMMETRIES IN THE COMPLEX FOCK MATRIX

In this section, we prove that, for a basis set of purely real functions, in pure RT-TDDFT (without Hartree–Fock exchange), the Fock matrix is purely real and symmetric and depends only on the real part of the complex density matrix. In the case of hybrid RT-TDDFT, however, the HF exchange term of the Fock matrix is complex Hermitian and depends on the full complex density matrix. The derivation presented is similar to that given in ref 36. For simplicity, we assume a closed shell system, but the results are identical for an open shell system.

Recall that in hybrid DFT–HF, the elements of the Fock matrix take the general form

$$\begin{aligned} F_{\mu\nu}[\mathbf{P}(t)] = & \mathbf{H}_{\mu\nu}^{\text{core}} + \mathbf{G}_{\mu\nu}^J(t) + \alpha \mathbf{G}_{\mu\nu}^K(t) + \beta \mathbf{G}_{\mu\nu}^{\text{X-DFT}}(t) \\ & + \gamma \mathbf{G}_{\mu\nu}^{\text{C-DFT}}(t) + \mathbf{V}^{\text{app}}(t) \end{aligned} \quad (37)$$

where  $\mu$  and  $\nu$  are indexes for the atomic orbitals,  $\mathbf{H}^{\text{core}}$  is the time-independent one-electron part,  $\mathbf{G}^J(t)$  and  $\mathbf{G}^K(t)$  are the time-dependent Coulomb and exchange terms,  $\mathbf{G}^{\text{X-DFT}}$  and  $\mathbf{G}^{\text{C-DFT}}$  are the DFT exchange and correlation terms, and  $\mathbf{V}^{\text{app}}(t)$  is the potential due to an external perturbation (e.g. electric field). In RT-TDDFT, the Fock matrix  $\mathbf{F}(t)$  and the density matrix  $\mathbf{P}$  are in general complex and Hermitian. We will discuss the symmetries in eq 37 term by term.

First, we note that the applied potential  $\mathbf{V}^{\text{app}}(t)$  is independent of the density matrix, and for all physical potentials, it is purely real. This is not true in the case of nonphysical potentials such as complex absorbing boundary conditions, but in such situations, the Fock matrix ceases to be Hermitian and the total system charge is not conserved in time, which requires a careful reformulation of TDDFT.

The time-independent one-electron part  $\mathbf{H}^{\text{core}}$  includes kinetic and electron–nuclear terms

$$\mathbf{H}_{\mu\nu}^{\text{core}} = \mathbf{T}_{\mu\nu} + \mathbf{V}_{\mu\nu}^{\text{eN}} \quad (38)$$

$$= \int d\mathbf{r}_1 \phi_{\mu}(\mathbf{r}_1) \left[ -\frac{1}{2} \nabla_1^2 \right] \phi_{\nu}(\mathbf{r}_1) + \int d\mathbf{r}_1 \phi_{\nu}(\mathbf{r}_1) \left[ -\sum_A \frac{Z_A}{|\mathbf{r}_1 - \mathbf{R}_A|} \right] \phi_{\mu}(\mathbf{r}_1) \quad (39)$$

where  $\{\phi(\mathbf{r})\}$  are the atomic orbitals which we henceforth assume are real. Since this expression is independent of the density matrix, and the integrals in eq 39 are symmetric with respect to the exchange of  $\mu$  and  $\nu$ , the core term is pure real and symmetric.

Next, in adiabatic RT-TDDFT, the DFT exchange and correlation terms are all functionals uniquely determined by the instantaneous charge density (and possibly its gradients):

$$\mathbf{G}_{\mu\nu}^{\text{X-DFT}} = \mathbf{G}_{\mu\nu}^{\text{X-DFT}}[\rho(\mathbf{r}, t)] \quad (40)$$

$$\mathbf{G}_{\mu\nu}^{\text{C-DFT}}(t) = \mathbf{G}_{\mu\nu}^{\text{C-DFT}}[\rho(\mathbf{r}, t)] \quad (41)$$

The charge density  $\rho(\mathbf{r}, t)$  is dependent only on the real part of the density matrix

$$\rho(\mathbf{r}, t) = \sum_{\mu} \sum_{\nu} \text{Re}[\mathbf{P}_{\mu\nu}(t)] \phi_{\mu}(\mathbf{r}) \phi_{\nu}(\mathbf{r}) \quad (42)$$

and therefore the DFT XC terms are both real and symmetric and depend only on the real part of  $\mathbf{P}_{\mu\nu}(t)$ .

The Coulomb term takes the form

$$\mathbf{G}_{\mu\nu}^J(t) = \sum_{\lambda\sigma} \mathbf{P}_{\lambda\sigma}(t) (\mu\nu|\sigma\lambda) \quad (43)$$

where  $(\mu\nu|\sigma\lambda)$  are the standard two-electron integrals

$$(\mu\nu|\sigma\lambda) \equiv \int \phi_{\mu}(\mathbf{r}_1) \phi_{\nu}(\mathbf{r}_1) \frac{1}{r_{12}} \phi_{\sigma}(\mathbf{r}_2) \phi_{\lambda}(\mathbf{r}_2) d\mathbf{r}_1 d\mathbf{r}_2 \quad (44)$$

Note that since the basis functions are real, these two-electron integrals are symmetric to permutation of  $\lambda$  and  $\sigma$ :

$$(\mu\nu|\sigma\lambda) = (\mu\nu|\lambda\sigma) = (\nu\mu|\lambda\sigma) = (\nu\mu|\sigma\lambda) \quad (45)$$

The double sum in eq 43 can be split into three parts

$$\mathbf{G}_{\mu\nu}^J(t) = \sum_{\lambda} \sum_{\sigma < \lambda} \mathbf{P}_{\lambda\sigma}(t) (\mu\nu|\sigma\lambda) + \sum_{\lambda} \mathbf{P}_{\lambda\lambda}(t) (\mu\nu|\lambda\lambda) + \sum_{\lambda} \sum_{\sigma > \lambda} \mathbf{P}_{\lambda\sigma}(t) (\mu\nu|\sigma\lambda) \quad (46)$$

Swapping the indices of summation for the third term gives

$$\mathbf{G}_{\mu\nu}^J(t) = \sum_{\lambda} \sum_{\sigma < \lambda} \mathbf{P}_{\lambda\sigma}(t) (\mu\nu|\sigma\lambda) + \sum_{\lambda} \mathbf{P}_{\lambda\lambda}(t) (\mu\nu|\lambda\lambda) + \sum_{\sigma} \sum_{\sigma' > \lambda} \mathbf{P}_{\sigma\lambda}(t) (\mu\nu|\lambda\sigma) \quad (47)$$

and using the symmetry of the two-electron integrals (eq 45), the Coulomb matrix elements become

$$\mathbf{G}_{\mu\nu}^J(t) = \sum_{\sigma < \lambda} [\mathbf{P}_{\lambda\sigma}(t) + \mathbf{P}_{\sigma\lambda}(t)] (\mu\nu|\sigma\lambda) + \sum_{\lambda} \mathbf{P}_{\lambda\lambda}(t) (\mu\nu|\lambda\lambda) \quad (48)$$

The real part is

$$\text{Re}[\mathbf{G}_{\mu\nu}^J(t)] = \sum_{\sigma < \lambda} \{ \text{Re}[\mathbf{P}_{\lambda\sigma}(t)] + \text{Re}[\mathbf{P}_{\sigma\lambda}(t)] \} (\mu\nu|\sigma\lambda) + \sum_{\lambda} \text{Re}[\mathbf{P}_{\lambda\lambda}(t)] (\mu\nu|\lambda\lambda) \quad (49)$$

but since  $\mathbf{P}$  is Hermitian, the real part is symmetric, which gives

$$\text{Re}[\mathbf{G}_{\mu\nu}^J(t)] = 2 \sum_{\sigma < \lambda} \text{Re}[\mathbf{P}_{\lambda\sigma}(t)] (\mu\nu|\sigma\lambda) + \sum_{\lambda} \text{Re}[\mathbf{P}_{\lambda\lambda}(t)] (\mu\nu|\lambda\lambda) \quad (50)$$

Equation 50 is symmetric to the exchange of  $\mu$  and  $\nu$ ; thus  $\text{Re}[\mathbf{G}_{\mu\nu}^J(t)] = \text{Re}[\mathbf{G}_{\nu\mu}^J(t)]$ , and the real part of the Coulomb term is symmetric. The imaginary part is

$$\text{Im}[\mathbf{G}_{\mu\nu}^J(t)] = \sum_{\sigma < \lambda} \text{Im}\{ \mathbf{P}_{\lambda\sigma}(t) + \mathbf{P}_{\sigma\lambda}(t) \} (\mu\nu|\sigma\lambda) + \sum_{\lambda} \text{Im}[\mathbf{P}_{\lambda\lambda}(t)] (\mu\nu|\lambda\lambda) \quad (51)$$

but here due to Hermiticity the imaginary part of the density matrix is antisymmetric with on-diagonal elements of zero; thus

$$\text{Im}[\mathbf{P}_{\lambda\sigma}(t)] + \text{Im}[\mathbf{P}_{\sigma\lambda}(t)] = 0 \quad (52)$$

$$\text{Im}[\mathbf{P}_{\lambda\lambda}(t)] = 0 \quad (53)$$

and the imaginary part of the Coulomb matrix vanishes

$$\text{Im}[\mathbf{G}_{\mu\nu}^J(t)] = 0 \quad (54)$$

Thus, the Coulomb term is a real-valued symmetric matrix which only depends on the real part of the complex density matrix.

A similar analysis can be done for the exchange matrix,

$$\mathbf{G}_{\mu\nu}^K(t) = \sum_{\lambda\sigma} \mathbf{P}_{\lambda\sigma}(t) (\mu\lambda|\sigma\nu) \quad (55)$$

(note the different two electron integrals from Coulomb part), which after expanding into three terms and swapping summation in the third term gives

$$\mathbf{G}_{\mu\nu}^K(t) = \sum_{\lambda} \sum_{\sigma < \lambda} \mathbf{P}_{\lambda\sigma}(t) (\mu\lambda|\sigma\nu) + \sum_{\lambda} \mathbf{P}_{\lambda\lambda}(t) (\mu\lambda|\sigma\nu) + \sum_{\sigma} \sum_{\sigma' < \lambda} \mathbf{P}_{\sigma\lambda}(t) (\mu\lambda|\sigma\nu) \quad (56)$$

The real part is

$$\begin{aligned} \text{Re}[\mathbf{G}_{\mu\nu}^K(t)] &= \sum_{\sigma < \lambda} \text{Re}[\mathbf{P}_{\lambda\sigma}(t)](\mu\lambda|\sigma\nu) + \sum_{\lambda} \text{Re}[\mathbf{P}_{\lambda\lambda}(t)](\mu\lambda|\lambda\nu) \\ &\quad + \sum_{\sigma < \lambda} \text{Re}[\mathbf{P}_{\sigma\lambda}(t)](\mu\sigma|\lambda\nu) \end{aligned} \quad (57)$$

$$\begin{aligned} &= \sum_{\sigma < \lambda} \text{Re}[\mathbf{P}_{\lambda\sigma}(t)](\mu\lambda|\sigma\nu) + (\mu\sigma|\lambda\nu) \\ &\quad + \sum_{\lambda} \text{Re}[\mathbf{P}_{\lambda\lambda}(t)](\mu\lambda|\lambda\nu) \end{aligned} \quad (58)$$

To check the symmetry, we switch the  $\mu$  and  $\nu$  indices

$$\text{Re}[\mathbf{G}_{\nu\mu}^K(t)] = \sum_{\sigma < \lambda} \text{Re}[\mathbf{P}_{\lambda\sigma}(t)](\nu\lambda|\sigma\mu) + (\nu\sigma|\lambda\mu) + \sum_{\lambda} \text{Re}[\mathbf{P}_{\lambda\lambda}(t)](\nu\lambda|\lambda\mu) \quad (59)$$

Permuting the two electron integrals (eq 45) gives

$$\text{Re}[\mathbf{G}_{\nu\mu}^K(t)] = \sum_{\sigma < \lambda} \text{Re}[\mathbf{P}_{\lambda\sigma}(t)](\mu\sigma|\lambda\nu) + (\mu\lambda|\sigma\nu) + \sum_{\lambda} \text{Re}[\mathbf{P}_{\lambda\lambda}(t)](\mu\lambda|\lambda\nu) \quad (60)$$

$$= \text{Re}[\mathbf{G}_{\nu\mu}^K(t)] \quad (61)$$

thus the real part of the exchange term is symmetric. The imaginary part is (c.f. eq 57)

$$\begin{aligned} \text{Im}[\mathbf{G}_{\mu\nu}^K(t)] &= \sum_{\sigma < \lambda} \text{Im}[\mathbf{P}_{\lambda\sigma}(t)](\mu\lambda|\sigma\nu) + \sum_{\lambda} \text{Im}[\mathbf{P}_{\lambda\lambda}(t)](\mu\lambda|\lambda\nu) \\ &\quad + \sum_{\sigma < \lambda} \text{Im}[\mathbf{P}_{\sigma\lambda}(t)](\mu\sigma|\lambda\nu) \end{aligned} \quad (62)$$

and since  $\mathbf{P}(t)$  is Hermitian, the imaginary part is antisymmetric and has zeros on the on-diagonal. Therefore

$$\text{Im}[\mathbf{G}_{\mu\nu}^K(t)] = \sum_{\sigma < \lambda} \text{Im}[\mathbf{P}_{\lambda\sigma}(t)][(\mu\lambda|\sigma\nu) - (\mu\sigma|\lambda\nu)] \quad (63)$$

As before, we examine the symmetry by swapping  $\mu$  and  $\nu$

$$\text{Im}[\mathbf{G}_{\nu\mu}^K(t)] = \sum_{\sigma < \lambda} \text{Im}[\mathbf{P}_{\lambda\sigma}(t)][(\nu\lambda|\sigma\mu) - (\nu\sigma|\lambda\mu)] \quad (64)$$

$$= \sum_{\sigma < \lambda} \text{Im}[\mathbf{P}_{\lambda\sigma}(t)][(\mu\sigma|\lambda\nu) - (\mu\lambda|\sigma\nu)] \quad (65)$$

$$= -\text{Im}[\mathbf{G}_{\mu\nu}^K(t)] \quad (66)$$

where again we used the permutation of the two-electron integrals. Therefore, the exchange term is complex, Hermitian, and depends on the full complex density matrix.

## AUTHOR INFORMATION

### Corresponding Author

\*E-mail: kenneth.lopata@pnl.gov; niri.govind@pnl.gov.

## ACKNOWLEDGMENT

The research was performed using EMSL, a national scientific user facility sponsored by the U.S. Department of Energy's Office of Biological and Environmental Research and located at Pacific Northwest National Laboratory (PNNL). PNNL is operated for the Department of Energy by the Battelle Memorial Institute under Contract DE-AC06-76RLO-1830. KL acknowledges the

William Wiley Postdoctoral Fellowship from EMSL. Discussions with Daniel Neuhauser, Karol Kowalski, Hongfei Wang, Eric Bylaska, Bert de Jong, and Bill Shelton are gratefully acknowledged.

## REFERENCES

- (1) Runge, E.; Gross, E. K. U. *Phys. Rev. Lett.* **1984**, *52*, 997.
- (2) Petersilka, M.; Gossmann, U. J.; Gross, E. K. U. *Phys. Rev. Lett.* **1996**, *76*, 1212–1215.
- (3) Casida, M. E. In *Recent advances in density functional methods*; Chong, D. P., Ed.; World Scientific Publishing: River Edge, NJ, 1995; Vol. 1, Chapter 5, pp 155–192.
- (4) Burke, K.; Werschnik, J.; Gross, E. K. U. *J. Chem. Phys.* **2005**, *123*, 062206.
- (5) Harumiya, K.; Kawata, I.; Kono, H.; Fujimura, Y. *J. Chem. Phys.* **2000**, *113*, 8953–8960.
- (6) Krause, P.; Klamroth, T.; Saalfrank, P. *J. Chem. Phys.* **2005**, *123*, 074105.
- (7) Greenman, L.; Ho, P. J.; Pabst, S.; Kamarchik, E.; Mazziotti, D. A.; Santra, R. *Phys. Rev. A* **2010**, *82*, 023406.
- (8) Deb, B.; Ghosh, S. *J. Chem. Phys.* **1982**, *77*, 342.
- (9) Doms, A.; Reinhard, P.-G.; Suraud, E. *Phys. Rev. Lett.* **1998**, *80*, 5520–5523.
- (10) Kulander, K. C. *Phys. Rev. A* **1987**, *36*, 2726–2738.
- (11) Li, X.; Smith, S.; Markevitch, A.; Romanov, D.; Levis, R.; Schlegel, H. *Phys. Chem. Chem. Phys.* **2005**, *7*, 233–239.
- (12) Bartell, L.; Wall, M.; Neuhauser, D. *J. Chem. Phys.* **2010**, *132*, 234106.
- (13) Theilhaber, J. *Phys. Rev. B* **1992**, *46*, 12990–13003.
- (14) Yabana, K.; Bertsch, G. F. *Phys. Rev. B* **1996**, *54*, 4484–4487.
- (15) Baer, R.; Gould, R. J. *Chem. Phys.* **2001**, *114*, 3385–3392.
- (16) Pi, M.; Ancilotto, F.; Lipparini, E.; Mayol, R. *Physica E* **2004**, *24*, 297–307.
- (17) Castro, A.; Appel, H.; Oliveira, M.; Rozzi, C. A.; Andrade, X.; Lorenzen, F.; Marques, M. A. L.; Gross, E. K. U.; Rubio, A. *Phys. Status Solidi B* **2006**, *243*, 2465–2488.
- (18) Sugino, O.; Miyamoto, Y. *Phys. Rev. B* **1999**, *59*, 2579–2586.
- (19) Baer, R.; Neuhauser, D.; Weiss, S. *Nano Lett.* **2004**, *4*, 85–88.
- (20) Qian, X.; Li, J.; Lin, X.; Yip, S. *Phys. Rev. B* **2006**, *73*, 035408.
- (21) Soler, J.; Artacho, E.; Gale, J.; García, A.; Junquera, J.; Ordejón, P.; Sánchez-Portal, D. *J. Phys.: Condens. Mater.* **2002**, *14*, 2745.
- (22) Tsolakidis, A.; Sánchez-Portal, D.; Martin, R. M. *Phys. Rev. B* **2002**, *66*, 235416.
- (23) Takimoto, Y.; Vila, F. D.; Rehr, J. J. *J. Chem. Phys.* **2007**, *127*, 154114.
- (24) Meng, S.; Kaxiras, E. *J. Chem. Phys.* **2008**, *129*, 054110.
- (25) Niehaus, T. A.; Suhai, S.; Della Sala, F.; Lugli, P.; Elstner, M.; Seifert, G.; Frauenheim, T. *Phys. Rev. B* **2001**, *63*, 085108.
- (26) Wang, F.; Yam, C. Y.; Chen, G.; Wang, X.; Fan, K.; Niehaus, T. A.; Frauenheim, T. *Phys. Rev. B* **2007**, *76*, 045114.
- (27) Cheng, C.-L.; Evans, J. S.; Van Voorhis, T. *Phys. Rev. B* **2006**, *74*, 155112.
- (28) Evans, J. S.; Voorhis, T. V. *Nano Lett.* **2009**, *9*, 2671–2675.
- (29) Li, X.; Tully, J. C. *Chem. Phys. Lett.* **2007**, *439*, 199–203.
- (30) Sun, J.; Song, J.; Zhao, Y.; Liang, W.-Z. *J. Chem. Phys.* **2007**, *127*, 234107.
- (31) Isborn, C. M.; Li, X. *J. Chem. Phys.* **2008**, *129*, 204107.
- (32) Isborn, C. M.; Li, X. *J. Chem. Theory Comput.* **2009**, *9*, 2415–2419.
- (33) Micha, D. A.; Runge, K. *Phys. Rev. A* **1994**, *50*, 322–336.
- (34) Li, X.; Tully, J. C.; Schlegel, H. B.; Frisch, M. J. *J. Chem. Phys.* **2005**, *123*, 084106.
- (35) Livshits, E.; Baer, R. *J. Phys. Chem. A* **2006**, *110*, 8443–8450.
- (36) Jakowski, J.; Morokuma, K. *J. Chem. Phys.* **2009**, *130*, 224106.
- (37) Tully, J. C. *J. Chem. Phys.* **1990**, *93*, 1061–1071.
- (38) Craig, C. F.; Duncan, W. R.; Prezhdov, O. V. *Phys. Rev. Lett.* **2005**, *95*, 163001.



- (39) Duncan, W. R.; Stier, W. M.; Prezhdo, O. V. *J. Am. Chem. Soc.* **2005**, *127*, 7941–7951.
- (40) Zhang, X.; Li, Z.; Lu, G. *Phys. Rev. B* **2010**, *82*, 205210.
- (41) Stella, L.; Meister, M.; Fisher, A. J.; Horsfield, A. P. *J. Chem. Phys.* **2007**, *127*, 214104.
- (42) Valiev, M.; Bylaska, E.; Govind, N.; Kowalski, K.; Straatsma, T.; Dam, H. V.; Wang, D.; Nieplocha, J.; Apra, E.; Windus, T.; de Jong, W. *Comput. Phys. Commun.* **2010**, *181*, 1477–1489.
- (43) Baer, R.; Neuhauser, D. *Phys. Rev. Lett.* **2005**, *94*, 043002.
- (44) Livshits, E.; Baer, R. *Phys. Chem. Chem. Phys.* **2007**, *9*, 2932–2941.
- (45) Baer, R. *THEOCHEM* **2009**, *914*, 19–21.
- (46) Baer, R.; Neuhauser, D. *J. Chem. Phys.* **2004**, *121*, 9803–9807.
- (47) Yabana, K.; Nakatsukasa, T.; Iwata, J.; Bertsch, G. *Phys. Status Solidi B* **2006**, *243*, 1121–1138.
- (48) Neuhauser, D.; Lopata, K. *J. Chem. Phys.* **2008**, *129*, 134106.
- (49) Becke, A. *J. Chem. Phys.* **1993**, *98*, 5648–5652.
- (50) Dreuw, A.; Weisman, J.; Head-Gordon, M. *J. Chem. Phys.* **2003**, *119*, 2943.
- (51) Vydrov, O.; Heyd, J.; Krukau, A.; Scuseria, G. *J. Chem. Phys.* **2006**, *125*, 074106.
- (52) Jacquemin, D.; Perpète, E. A.; Scuseria, G. E.; Ciofini, I.; Adamo, C. *Chem. Phys. Lett.* **2008**, *465*, 226–229.
- (53) Yanai, T.; Tew, D. P.; Handy, N. C. *Chem. Phys. Lett.* **2004**, *393*, 51–57.
- (54) Govind, N.; Valiev, M.; Jensen, L.; Kowalski, K. *J. Phys. Chem. A* **2009**, *113*, 6041–6043.
- (55) (a) Jensen, L.; Govind, N. *J. Phys. Chem. A* **2009**, *113*, 9761–9765. (b) Jensen, L.; Govind, N. *J. Phys. Chem. A* **2009**, *113*, 11095–11095.
- (56) Baer, R.; Livshits, E.; Salzner, U. *Annu. Rev. Phys. Chem.* **2010**, *61*, 85–109.
- (57) Kosloff, R. *J. Phys. Chem.* **1988**, *92*, 2087–2100.
- (58) Liu, J.; Guo, Z.; Sun, J.; Liang, W. *Front. Chem. China* **2010**, *5*, 11–28.
- (59) Castro, A.; Marques, M. A. L.; Rubio, A. *J. Chem. Phys.* **2004**, *121*, 3425–3433.
- (60) Magnus, W. *Commun. Pure Appl. Math.* **1954**, *7*, 649–673.
- (61) de Jong, W. A.; Bylaska, E.; Govind, N.; Janssen, C. L.; Kowalski, K.; Müller, T.; Nielsen, I. M. B.; van Dam, H. J. J.; Veryazov, V.; Lindh, R. *Phys. Chem. Chem. Phys.* **2010**, *12*, 6896–6920.
- (62) Eichkorn, K.; Treutler, O.; Ošhm, H.; Hašser, M.; Ahlrichs, R. *Chem. Phys. Lett.* **1995**, *240*, 283–289.
- (63) EMSL Basis Set Exchange. <https://bse.pnl.gov> (accessed Dec 10, 2010).
- (64) Tretiak, S.; Isborn, C. M.; Niklasson, A. M. N.; Challacombe, M. *J. Chem. Phys.* **2009**, *130*, 054111.
- (65) Tsien, R. *Annu. Rev. Biochem.* **1998**, *67*, 509–544.
- (66) Dong, J.; Solntsev, K. M.; Tolbert, L. M. *J. Am. Chem. Soc.* **2006**, *128*, 12038–12039.
- (67) Kowalski, K.; Krishnamoorthy, S.; Villa, O.; Hammond, J.; Govind, N. *J. Chem. Phys.* **2010**, *132*, 154103.
- (68) Sadlej, A. *Collect. Czech. Chem. Commun.* **1988**, *53*, 1995–2016.
- (69) Mozer, A. J.; Griffith, M. J.; Tsekouras, G.; Wagner, P.; Wallace, G. G.; Mori, S.; Sunahara, K.; Miyashita, M.; Earles, J. C.; Gordon, K. C.; Du, L.; Katoh, R.; Furube, A.; Officer, D. L. *J. Am. Chem. Soc.* **2009**, *131*, 15621–15623.
- (70) Maligaspe, E.; Sandanayaka, A. S. D.; Hasobe, T.; Ito, O.; D'Souza, F. *J. Am. Chem. Soc.* **2010**, *132*, 8158–8164.
- (71) Palumbo, M.; Hogan, C.; Sottile, F.; Bagalá, P.; Rubio, A. *J. Chem. Phys.* **2009**, *131*, 084102.
- (72) Iikura, H.; Tsuneda, T.; Yanai, T.; Hirao, K. *J. Chem. Phys.* **2001**, *115*, 3540–3544.
- (73) Samoylova, E.; Schultz, T.; Hertel, I.; Radloff, W. *Phys. Chem.* **2008**, *347*, 376–382.
- (74) Szabo, A.; Ostlund, N. *Modern Quantum Chemistry*; Dover Publications: Mineola, NY, 1996; pp 142–145.
- (75) *Blender*; The Blender Foundation: Amsterdam, The Netherlands, 2010.